Accepted for publication in *Building and Environment* on December 4, 2014

CFD analysis of cross-ventilation of a generic isolated building with asymmetric opening positions: impact of roof angle and opening location

J.I. Peren [a,b,1], T. van Hooff [c], B.C.C. Leite, [a], B. Blocken [b,c]

[a] Civil Construction Engineering Department, Polytechnic School of the University of São Paulo - USP, Av. Prof. Luciano Gualberto, travessa 2 nº 83 - CEP 05508-900 - São Paulo - SP, Brazil.
[b] Building Physics and Services, Eindhoven University of Technology, P.O. Box 513, 5600 MB Eindhoven, The Netherlands.
[c] Building Physics Section, Katholieke Universiteit Leuven, Kasteelpark Arenberg 40, P.O. Box 2447, 3001 Leuven, Belgium.

Graphical abstract

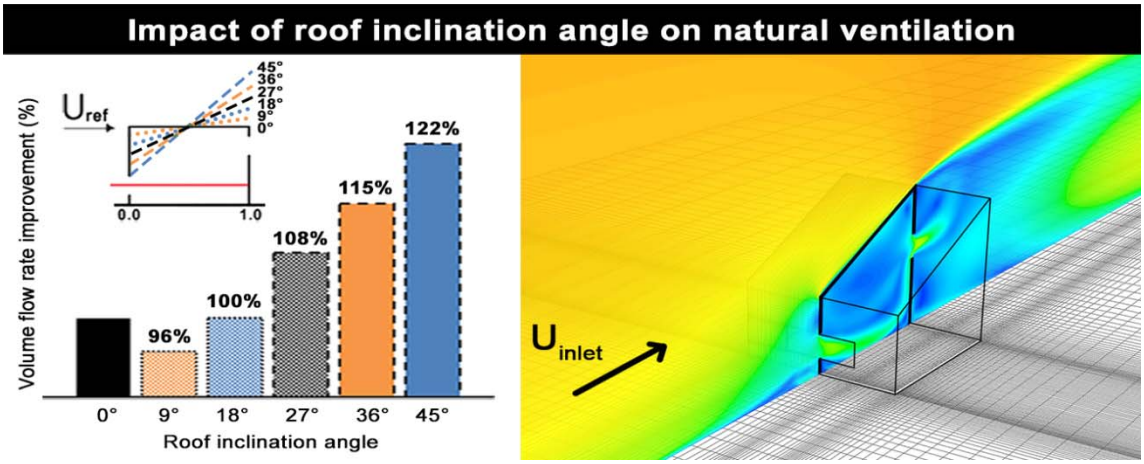

Highlights

- CFD simulations of cross ventilation with 3D steady RANS and various turbulence models.
- Influence of roof inclination angle and outlet opening position.
- Grid-sensitivity analysis and validation with PIV measurements.
- SST k-ω model and RNG k-ε model show best performance.
- Roof inclination angle has much larger effect than position of outlet opening.

[1] Corresponding author: E-mail address: j.i.peren.montero@tue.nl. Tel.: +31 (0) 40 247 3667. Fax +31 (0)40 243 8595. PO Box 513, 5600 MB, Eindhoven.

Abstract

The position of window openings and roof inclination are important parameters determining the effectiveness of wind-driven cross-ventilation in buildings. Many studies on natural ventilation have been performed in the past, however, a detailed review of the literature indicates that the majority of these studies focused on flat roofs with symmetric opening positions. There is a lack of research that analyses the impact of asymmetric opening positions and roof inclination on natural ventilation potential. This paper presents Computational Fluid Dynamics (CFD) simulations to analyze the natural ventilation flow in a generic isolated building with different vertical positions of the outlet opening – yielding asymmetric opening positions – and five different roof inclination angles. The simulations are performed using the 3D steady Reynolds-Averaged Navier-Stokes (RANS) equations. They are based on a grid-sensitivity analysis and on validation with previously published wind-tunnel measurements using Particle Image Velocimetry. The results show that the shear-stress transport (SST) k-ω and the Renormalization-group (RNG) k-ε turbulence models provide the best agreement with the experimental data. It is also shown that the roof inclination angle has a significant effect on the ventilation flow; the volume flow rate increases by more than 22%. The maximum local indoor air velocity increases considerably when the inclination angle is increased, however, the differences in the average velocity in the occupied zone are only around 7%. The vertical position of the outlet opening has a relatively small impact on the volume flow rate (less than 4%), and a small influence on the average velocity in the occupied zone (< 5%).

Keywords: Computational Fluid Dynamics (CFD); Building geometry; Natural ventilation; Model validation; Urban physics; Building aerodynamics.

1 Introduction

A sawtooth roof on buildings can contribute to a sustainable and healthy indoor environment as it can allow additional daylight and natural ventilation compared to a standard flat roof. Sawtooth-roof buildings have lower level openings in the (windward) facade and also upper-level openings near the roof top in the opposite (leeward) facade. Using the upper-level openings located near the roof, the sawtooth roof can achieve more uniform and higher daylight intensity levels than the levels obtained by an opening located in the middle or in the lower part of a facade [1]. When the upper-level opening captures the wind the sawtooth roof is called "wind catcher" and, when it is used to extract indoor air from the building using the underpressure region in the wake of a building it is called a "leeward sawtooth roof" [2]. A sawtooth roof can be employed in different types of buildings, such as schools [3–5], low-rise industrial buildings [6] and hospitals [7]. Although sawtooth roofs have a great potential to increase natural ventilation, especially in hot climates, their design is not well explored and they are still not applied on a large scale [2].

When a sawtooth roof is oriented as leeward sawtooth roof , the wind-driven natural ventilation is improved [8] and it has several advantages compared to a flat roof: (a) it can facilitate upward cross-ventilation (low-level supply and upper-level extraction) using wind and buoyancy as driving forces for the ventilation flow; (b) it can work as part of a hybrid ventilation system, such as displacement ventilation (DV) [9] or under-floor air distribution (UFAD) system, enabling the achievement of thermal comfort in a more energy-efficient way by using wind and buoyancy as driving forces instead of fans as much as possible. The ventilation efficiency of a building with a sawtooth roof depends among others on its orientation with respect to the oncoming wind flow. In addition, the impact of many other building parameters, such as roof height and shape and inlet-outlet opening configuration (size and vertical position), have, to the best knowledge of the authors, not yet been thoroughly investigated.

Several studies have been conducted on wind-induced loads on gable roofs [10–12], arched roofs [13], mono-sloped roofs or shed roofs [14,15], various other roof geometries [16,17] and multi-span roofs such as sawtooth roofs [6,15]. The findings reported in these publications are useful for the understanding of the building aerodynamics and they provide some information on the potential for wind-driven cross-ventilation. In general, wind-driven cross-ventilation studies for low rise-buildings can be organized in four groups: (1) buildings with a flat roof and symmetric opening positions; i.e. inlet and outlet opening at the same height in the windward and leeward building facade; (2) buildings with a flat roof and asymmetric opening positions; (3) buildings with a pitched roof and symmetric opening positions; (4) buildings with a pitched roof and asymmetric opening positions. Many research efforts focused on group (1) (e.g. [18–30]). Within this group, there are studies on the effect of the opening size (wall porosity) [19,21,23,26,27,29], the inlet-outlet opening ratio and location [21,23,25,27,29] and the building aspect ratio [22,28]. Less studies focused on buildings with a flat roof and with asymmetric opening positions located in the facade (group 2); some examples are [23,25-27]. Several studies

analyzed the influence of the roof shape but with symmetric opening positions (in terms of height in the facade; group 3) [31–36]. Finally, quite some studies focused on buildings with a pitched roof and asymmetric opening positions (group 4) (e.g. ([37-50]). Within this group however, only one study considered a saw-tooth roof [45]. In addition, there are some related studies on wind towers, wind catchers, venturi-shaped roofs or other constructions on the roof (e.g. [39,51–60]). This review of the literature shows that almost no studies have been conducted on the effect of roof inclination in combination with asymmetric positions of the vertical openings in the building facade.

Therefore, in this paper, the impact of the roof inclination angle and the vertical location of the outlet opening on the mean velocity pattern and volume flow rate for a generic isolated building is analyzed using Computational Fluid Dynamics (CFD). A CFD analysis is required for this study since the performance assessment of the different roof geometries is not only based on the volume flow rates through the windows, but also on the airflow pattern (velocities) inside the building resulting from the cross-ventilation flow. If only the volume flow rates would be of interest one could consider performing CFD simulations of a sealed building, and subsequently using the pressure coefficients and an estimated discharge coefficient to calculate the volume flow rates. It must be noted that the value of the discharge coefficient depends on several factors and is difficult to accurately predict. The Reynolds number, the wind direction, etc. play a role in the determination of the discharge coefficient (e.g. [61]), as well as the presence or absence of "flow contact" in case of cross ventilation through large ventilation openings. When flow contact is present jet momentum is conserved and reaches the leeward opening, resulting in different values of the discharge coefficient for the windward and leeward opening (e.g. [62,63]). In the past 50 years, CFD has developed into a powerful tool for studies in urban physics and building aerodynamics [64], including natural ventilation in buildings, as demonstrated by review and overview papers [30,64–71]. In this paper, the coupled approach (e.g. [29,30,42,47,48,50,63,72]) is employed using the 3D steady Reynolds-Averaged Navier-Stokes (RANS) equations. The coupled approach enables a detailed analysis of the indoor and outdoor airflow by performing one CFD simulation in which the indoor and outdoor airflow are modeled simultaneously and in the same computational domain. The detailed and high-quality Particle Image Velocimetry (PIV) wind-tunnel measurements provided by Karava et al. [27] for a generic isolated building with asymmetric opening positions and a flat roof are used for model validation. First, the PIV measurements are described in Section 2. Then, the numerical model for the validation case is presented in Section 3 and the validation results in Section 4, after which the sensitivity analyses are outlined in Section 5. Section 6 presents the CFD simulation results for the cases with the different roof inclination angles and the different vertical positions of the outlet opening in the leeward facade. Discussion and conclusions are given in Sections 7 and 8.

2 Wind-tunnel experiment

Karava et al. [27] carried out PIV measurements of wind-induced cross-ventilation for a generic isolated building model with a flat roof and both symmetric and asymmetric opening positions in the open-circuit boundary layer wind tunnel at Concordia University, Montreal, Canada [73]. The wind-tunnel has a test section of 1.8 x 1.8 x 12 m^3 (W x H x L). The building models were made from 2 mm cast transparent polymethyl methacrylate (PMMA) sheet at a scale of 1:200. The models had dimensions 100 x 100 x 80 mm^3 (W x D x H) (reduced-scale) corresponding to full-scale dimensions 20 x 20 x 16 m^3 (W x D x H) (Fig. 1). The reduced-scale building-model openings had a fixed height of 18 mm (3.6 m full scale) and a variable width, providing a wall porosity (opening area divided by wall area) of 5%, 10% and 20%. Three opening positions were considered: bottom, middle and top, with the center of the opening at h = 20 mm, 40 mm and 60 mm, respectively. In this paper, the focus is on the building model with the inlet opening at the bottom of the windward facade (center at h = 20 mm) and the outlet opening at the top of the opposite (leeward) facade (center at h = 60 mm) and with a wall porosity of 10%, as shown in Figure 1a,b. The PIV measurements were conducted in the vertical center plane, as indicated in Figure 1c. The incident mean velocity and turbulence intensity profiles were measured in the empty wind tunnel at the turntable center with a hot-film probe in the test section. Measurement and use of incident profiles rather than approach-flow profiles is important for a reliable validation study [74,75]. The reference mean wind speed U_{ref} = 6.97 m/s and a reference turbulence intensity of 10% were measured at building height (H = z_{ref}). The turbulence intensity was about 17% near ground level (12 mm) and 5% at gradient height (738 mm). The reduced-scale aerodynamic roughness length was z_0 = 0.025 mm corresponding to z_0 = 0.005 m in full scale [27]. For more information related to the wind-tunnel experiments the reader is referred to [27].

3 CFD simulations: computational settings and parameters

The computational settings and parameters for the reference case are described in this section. These settings and parameters will also be used for the sensitivity analyses (grid resolution, turbulence model, inlet turbulent kinetic energy), which will be presented in Section 4.

3.1 Computational domain and grid

The computational domain and grid are constructed at reduced scale (1:200) to exactly resemble the wind-tunnel geometry. They adhere to the best practice guidelines by Franke et al. [76] and Tominaga et al. [77], apart from the upstream length, which is reduced to 3 times the height of the building to limit the development of unintended streamwise gradients [78,79]. The dimensions of the domain are 0.9 x 1.54 x 0.48 m^3 (W x D x H) which correspond to 180 x 308 x 96 m^3 in full scale. The computational grid is fully structured and it is created using the surface-grid extrusion technique described by van Hooff and Blocken [47]. This technique allows full control of the size and shape of every grid cell and has been used successfully in previous studies for simple and complex building and urban geometries (e.g. [47,48,59,80-83]). The maximum stretching ratio is 1.2 and the first cell height is 2 mm at the building wall. A grid-sensitivity analysis is performed based on three grids (Fig. 2c-e); coarse, basic and fine grid, with 421,088 cells, 770,540 cells (reference case), and 1,607,572 cells, respectively. The results of the grid-sensitivity analysis are presented in Section 4.1.

3.2 Boundary conditions

At the inlet of the domain the approach-flow mean wind speed and turbulence profiles are imposed based on the wind-tunnel measurements. The inlet wind-velocity profile is defined according to the logarithmic law (Eq. 1):

$$U(z) = \frac{u^*_{ABL}}{\kappa} \ln\left(\frac{z + z_0}{z_0}\right) \quad (1)$$

where z_0 is the same as in the experiment and where u^*_{ABL} is the ABL friction velocity (= 0.35 m/s) that is determined based on the values of $U_{ref,}$ and z_{ref} from the experiment. Furthermore, κ is the von Karman constant (0.42) and z the height coordinate. The turbulent kinetic energy k is calculated from the mean wind speed and the measured turbulence intensity using Eq. (2):

$$k(z) = a(I_U(z)U(z))^2 \quad (2)$$

In this equation, I_u is the measured streamwise turbulence intensity and "a" is a parameter ranging from 0.5 to 1.5 [31,77]. The sensitivity of the results to the parameter "a" is tested and presented in Section 4.3. For the reference case a = 0.5. The turbulence dissipation rate ε is given by Eq. (3) and the specific dissipation rate ω by Eq. (4), where C_μ is an empirical constant taken equal to 0.09.

$$\varepsilon(z) = \frac{u^{*3}_{ABL}}{\kappa(z + z_0)} \quad (3)$$

$$\omega(z) = \frac{\varepsilon(z)}{C_\mu k(z)} \quad (4)$$

At the ground and building surfaces, the standard wall functions by Launder and Spalding [84] are used in conjunction with the sand-grain based roughness modification by Cebeci and Bradshaw [85]. For the ground surfaces, the values of the roughness parameters, i.e. the sand-grain roughness height (k_S = 0.28 mm) and the roughness constant (C_S = 0.874), are determined based on their relationship with the aerodynamic roughness length z_0 derived by Blocken et al. [78] (Eq. 5). For the building surface the value of the sand-grain roughness is zero (k_{Ss} = 0).

$$k_S = \frac{9.793 z_0}{C_S} \quad (5)$$

At the outlet plane, zero static pressure is applied and at the top and lateral sides of the domain a symmetry condition is imposed, i.e. zero normal velocity and zero normal gradients of all variables. As recommended by Blocken et al. [78,79], to assess the extent of unintended streamwise gradients (i.e. horizontal inhomogeneity) in the vertical profiles of mean wind speed and turbulent properties, a simulation in an empty computational domain is made using the shear-stress transport (SST) k-ω model [86]. The vertical profiles of U, k and ε at the inlet (inlet profiles) and at the building position (incident profiles) are shown in Figure 3, indicating that streamwise gradients are present but limited, especially for the mean wind speed profile.

3.3 Solver settings

The commercial CFD code ANSYS Fluent 12 [87] is used to perform the CFD simulations. The 3D steady Reynolds-Averaged Navier-Stokes (RANS) equations are solved in combination with the shear-stress transport (SST) k-ω model. The SIMPLE algorithm is used for pressure-velocity coupling, pressure interpolation is second order and second-order discretization schemes are used for both the convection terms and the viscous terms of the governing equations. Convergence is assumed to be obtained when all the scaled residuals leveled off and reached a minimum of 10^{-6} for x and y momentum, 10^{-5} for z momentum and 10^{-4} for k, ε and continuity. As also observed by Ramponi and Blocken [29,30], the simulations showed oscillatory convergence. To obtain a reliable steady value of the solution variables, the results are monitored over 10,400 iterations and the variables are calculated by averaging over 400 iterations (10,000-10,400), after the simulation reached a statistically stationary solution.

4 CFD simulations: validation

The results from the CFD simulations are compared with the PIV wind-tunnel experiments by Karava et al. [27]. The mean velocity vector field in the vertical center plane by PIV measurements and CFD simulations is shown in Figure 4a and 4b, respectively. The CFD simulations correctly predict the most important flow features such as the standing vortex upstream of the building and the flow pattern inside the building. Figure 4c and 4d compare the measured and computed streamwise wind speed ratio U/U_{ref} along a horizontal line going through the middle of the windward opening and along a diagonal line, indicating a good agreement. As pointed out by Ramponi and Blocken [30], the simulations overestimate the mean velocity around the opening, where the PIV measurements cannot provide accurate predictions due to reflections and shading effects [27]. Despite these differences an overall good agreement is observed.

5 CFD simulations: sensitivity analysis for computational parameters

A systematic sensitivity analysis for some of the computational parameters is conducted by varying one single parameter at a time compared to the reference case and comparing the results to those of the reference case. The following parameters are evaluated: (1) resolution of the computational grid (Subsection 4.1); (2) turbulence model (Subsection 4.2); and (3) inlet values of turbulent kinetic energy (Subsection 4.3). Table 1 provides an overview of the computational parameters for the sensitivity analysis with indication of the reference case in bold.

5.1 Impact of computational grid resolution

Performing a grid-sensitivity analysis is important to minimize the discretization errors and the computation time. In this study, a grid-sensitivity analysis was performed based on three grids: (1) a coarse grid with 421,088 cells; (2) a basic grid with 770,540 cells (reference case); and (3) a fine grid with 1,607,572 cells. The two additional grids (the coarser and the finer) were constructed by coarsening and refining the average grid with about a factor √2 in each direction. Figure 2 shows a perspective view of the three grids. Results of the grid-sensitivity analysis are shown in Figure 5, in terms of the streamwise wind speed ratio (U/U_{ref}) along a horizontal line going through the middle of the windward opening (Fig. 5a) and a diagonal line between the inlet and outlet opening (Fig. 5b). The results indicate that the basic grid (reference grid) provides nearly grid-independent results. In addition, the difference in the ventilation flow rate through the inlet opening is about 1% between the basic grid and the fine grid, and 7% between the basic and the coarse grid. Therefore, it is concluded that the basic grid is a suitable grid for this study and this grid is used in the remainder of this paper.

5.2 Impact of turbulence model

Turbulence model validation is of fundamental importance for the reliability of CFD simulations. 3D steady RANS simulations are carried out in combination with six turbulence models: (1) the standard k-ε model (Sk-ε) [88]; (2) the realizable k-ε model (Rk-ε) [89]; (3) the renormalization group k-ε model (RNG k-ε) [90,91]; (4) the standard k-ω model (Sk-ω) [92]; (5) the shear-stress transport k-ω model (SST k-ω) [86]; and (6) the Reynolds Stress Model (RSM) [93]. The impact of the six different turbulence models on the streamwise wind speed ratio (U/U_{ref}) is illustrated in Figure 6. The SST k-ω model (reference case) and the RNG k-ε model clearly provide the best agreement with the PIV measurements. Figure 6a shows that the differences between the turbulence models are most pronounced inside the building around x/D = 0.2 – 0.3.

In terms of the volume flow rate compared to that by the SST k-ω model (reference case), (= 0.0026 m^3/s), small deviations are observed for the RNG k-ε model (0.22%), the Sk-ε model (-0.05%) and the Sk-ω model (1.56%), with slightly larger deviations for the Rk-ε model (3.27%) and RSM (3.67%). Clearly, the volume flow rate deviations between the different turbulence models are very small. However, the deviation in indoor air velocity between the RNG k-ε and SST k-ω on the one hand, and the other turbulence models on the other hand, is very large (locally up to 300%). These large local differences can be explained by the different direction of the incoming jet flow. Note that in the majority of the previous studies on cross-ventilation in buildings with asymmetric openings, the Sk-ε turbulence model was used for the CFD simulations [25,37,39–43,45]. In addition, some studies were conducted using the RSM model (e.g. [25,40,43]), the realizable k-ε model (e.g. [25,47,48,50]), and the RNG k-ε model (e.g. [25,37,38]).

5.3 Impact of inlet turbulent kinetic energy

The values of turbulent kinetic energy (TKE) at the inlet of the domain can have a very large impact on the wind speed ratio inside the building [30]. The TKE profile at the inlet can be estimated from the measured wind velocity and turbulence intensity profiles. However, the turbulence intensity is often not measured is all three directions. If for example – as in this particular case - the only value measured in the wind tunnel is the longitudinal turbulence intensity ($I_u = \sigma_u/U$) this means that for the other components (σ_v and σ_w) assumptions have to be made. These assumptions can yield different values of the parameter a (in Eq. 2), ranging from 0.5 to 1.5. Here, simulations with these three values of a (0.5, 1 and 1.5) are performed and the resulting streamwise wind speed ratios (U/U_{ref}) are shown in Figure 7. It can be seen that there is a considerable influence of this value a on the mean velocities inside the building. Figure 7a clearly shows that the dimensionless velocity is overestimated inside the building for values of a larger than 0.5. The largest overestimations can be observed between $0 < x/D < 0.4$. They go up to a factor 4 when a = 1 and up to a factor 5 when a = 1.5. When a is taken equal to 1 and 1.5 the predicted volume flow rate is 7.2% and 8.7% higher than with a = 0.5, respectively. It can be concluded that the parameter a = 0.5 provides the best agreement with the experimental results. Although the best practice guidelines by Tominaga et al. [77] suggest using a = 1, and Ramponi and Blocken [30] confirmed that the value a = 1 is the best value for CFD simulations of a building with symmetric openings (inlet and outlet openings at the same height), in this particular study of a building with asymmetric opening positions (inlet and outlet opening at different heights), the most suitable value of the parameter a clearly appears to be 0.5.

6 CFD simulations: sensitivity analysis for geometrical parameters

The computational parameters and settings presented in the previous section, i.e., the basic grid resolution, the turbulence model (SST k-ω) and the parameter a (0.5), are employed in this section for the sensitivity analyses of roof inclination angle and the vertical location of the outlet opening.

6.1 Impact of roof inclination angle

To evaluate the impact of the roof inclination angle (RIA) on the ventilation flow, five roof inclination angles are studied for a normal wind incidence angle ($\varphi = 0°$): 9°, 18°, 27°, 36° and 45°. To allow a straightforward comparison that is not influenced by too many factors, the five cases have: (a) the same internal volume (0.0008 m^3 at reduced-scale); b) the same inlet and outlet opening size (consequently, each case has a different facade porosity); and (c) the same inlet and outlet opening location. Figure 8 shows the vertical cross-sections and computational grids of the reference case and the five additional cases with different roof inclination angles. Table 2 summarizes the cases and parameters. The cases are evaluated based on the volume flow rate and the mean wind speed ratio along a horizontal centerline going through the middle of the windward opening.

Figure 9 shows that the volume flow rate increases when increasing the roof inclination angle with more than 18° compared to the reference case. However, the volume flow rate for RIA_09 is only 96% of that of

RIA_00. The volume flow rate for RIA_18 is equal to that of RIA_00 (reference case). The volume flow rate for RIA_27 is 8% higher than RIA_00, for RIA_36 the increase is 15%, while for RIA_45 it is 22%.

Figure 10a shows that the streamwise wind speed ratio increases along almost the entire horizontal line when the roof inclination angle is increased, except for case RIA_09. Figure 10b shows that the indoor mean streamwise wind speed ratio along the horizontal line shows very large differences between the roof inclination angles, especially between $0.1 < x/D < 0.8$. Note that although case RIA_09 has a lower volume flow rate than the reference case, the indoor air velocity along the horizontal line is higher in some areas ($0.5 < x/D < 0.7$) than in the case with the flat roof. The streamwise wind speed ratio along the centerline is also locally higher than in the reference case for case RIA_18, despite the fact that the volume flow rate is equal in both cases. However, to provide a more overall judgment of the indoor air velocities, the non-dimensional area-averaged velocity magnitude ($|V|/U_{ref}$) in the occupied zone has been calculated for the vertical center plane. The height of the occupied zone is equal to the top of the windward opening. Table 3 provides the calculated values for all roof inclination angles. It can be seen that the non-dimensional average velocity magnitude in the occupied zone only shows small differences for the different roof inclination angles; all values are within a range of ± 7%, with the highest average velocity present for RIA_27. If the occupied zone is subdivided into two parts, a lower part (below windward window) and an upper part (from bottom to top of windward window), the effect of roof inclination angle on the jet flow direction through the window can be seen; for lower inclination angles the flow is directed more downwards, resulting in higher average velocities in the lower part of the occupied zone (up to 0.45 for RIA_09), whereas higher average velocities are present in the upper part of the occupied zone for large roof inclination angles, up to 0.34 for RIA_45. In order to further analyze the effect of the roof inclination and facade height on the flow pattern around and inside the building in more detail, Figure 11 shows contours of the pressure coefficient (C_P) and of the dimensionless velocity magnitude ($|V|/U_{ref}$). The pressure coefficient is calculated as:

$$C_P = \frac{(P - P_0)}{(0.5\rho U_{ref}{}^2)} \tag{6}$$

where P is the static pressure, P_0 the reference static pressure, $\rho = 1.225$ kg/m^3 the air density and U_{ref} is the approach-flow wind speed at building height ($U_{ref} = 6.97$ m/s at $z = 0.08$ m). It is shown that the overpressure above the inlet opening decreases monotonically when increasing the roof inclination angle, until the overpressures above and below the inlet opening become nearly equal. As a result of this different distribution of the pressure on the windward facade, the direction of the incoming jet flow slightly changes in each case, yielding a more horizontally oriented jet as the roof inclination angle increases. Figure 11 shows that the difference in underpressure behind the building between the different cases is higher than the overpressure difference in front of the building. This is an indication that the roof inclination angle is an important geometric parameter to increase wind-driven cross-ventilation.

It can be concluded that the case with a roof inclination angle of 45° results in the best ventilation performance. Nevertheless, it must be noted that this is also the case with the largest building height. Hence, building height could also be a parameter that increases the ventilation flow rate. This is in line with a previous study by Kindangen et al. [34], who found that roof height has a strong influence on the indoor airflow in buildings with wind-driven natural ventilation. However, in the study by Kindangen et al. [34], symmetric opening positions were considered (both openings at the same height).

6.2 Impact of outlet opening position

In order to evaluate the impact of the vertical position of the outlet opening, two additional cases are analyzed, RIA_27_B and RIA_45_B, and they are compared to the previously analyzed cases, RIA_27_A and RIA_45_A (Fig. 13). For RIA_27_B and RIA_45_B, the distance between the roof and the top of the outlet opening is the same as in the reference case.

The vertical position of the outlet opening only has a small impact on the volume flow rate. It increases with 4% from RIA_27_A to RIA_27_B and with 2% from RIA_45_A to RIA_45_B. Figure 13 shows that also the impact on the mean streamwise wind speed ratio on the horizontal center line is rather small. In addition, Table 4 shows the non-dimensional area-averaged velocity magnitude ($|V|/U_{ref}$) in the occupied zone in the vertical center plane for the above mentioned cases. It can be seen that the non-dimensional average velocity magnitudes in the entire occupied zone for the cases RIA_27_B and RIA_45_B are almost equal to the base case with a lower position of the leeward window; the differences between geometry A and B are 4.8% for RIA_27 and 0.4% for RIA_45.

Figure 14 shows the pressure coefficient (C_P) and non-dimensional velocity magnitude ($|V|/U_{ref}$) in the vertical center plane for RIA_27_A, RIA_27_B. Figure 15 shows the same variables for RIA_45_A and RIA_45_B. There are no significant differences between RIA_27_A and RIA_27_B, and also not between RIA_45_A and RIA_45_B. This finding is in line with the observation of Lo and Novoselac [94], who pointed out that the position of the outlet opening at the leeward facade only has a small impact on the volume flow rate, however, they analyzed a position of the outlet opening that is at the same level as the inlet opening, which is not the case in the current study.

7 Discussion

7.1 Driving pressure differences obtained from sealed building models

In an attempt to further analyze the reason for the large differences in the volume flow rate additional CFD simulations are performed for a sealed building model of RIA_00 and RIA_45. They provide information on the surface pressure coefficients at the locations where the windward and leeward opening would be located. Table 5 provides the C_P values for the windward ($C_{P;w}$) and leeward ($C_{P;l}$) opening location, as well as the pressure difference over the building (ΔC_P). The pressure difference (ΔC_P) for RIA_00 is 1.15, whereas it is equal to 1.31 for case RIA_45, which is an increase of 13%. The increase in volume flow rate for case RIA_45 could therefore partly be explained by the larger pressure difference over the building, i.e. a larger ΔC_P. However, Table 5 also shows ΔC_P for RIA_45_B, which is equal to 1.24. This value is a bit lower than the $\Delta C_P = 1.31$ for RIA_45_A, and would result in a lower volume flow rate for RIA_45_B when the orifice equation would be applied. However, the coupled simulations in subsection 6.2 indicated that the flow rate increased from RIA_45_A to RIA_45_B. This shows that the sealed-building pressure difference is not a good indicator for the actual volume flow rate. This is attributed to two reasons. First, for the different buildings, also the different flow resistance (through the openings and inside the building) will be different. Second, and probably more importantly, the sealed-building pressure difference is not necessarily equal to the actual driving pressure difference in the coupled simulation, especially for larger opening sizes (e.g. [95]). Indeed, in such cases, the sealed-building assumption does not hold (e.g. [63]). In addition, as stated in the introduction, the actual volume flow rate is difficult to obtain from the orifice equation due to the uncertainty in the discharge coefficients (e.g. [61,62,95]).

7.2 Limitations and future research

The two main goals of this study on upward wind-driven cross-ventilation are: (1) to evaluate the impact of the roof inclination angle and (2) to evaluate the impact of the vertical location of the outlet opening, both for a normal wind incidence angle ($\varphi = 0°$). Five roof inclination angles are evaluated (9°, 18°, 27°, 36° and 45°) and two of these cases (27° and 45°) are also used to analyze the impact of the vertical location of the outlet opening. It is essential to mention the limitations of the current study, which should be addressed in future research:

- This study considers a simplified single zone building. The impact of other building parameters such as eaves and internal layout must be investigated.
- This study is performed for an isolated building.
- The study focuses on one wind incidence angle ($\varphi = 0°$). The ventilation performance could change for other wind incidence angles.
- In this study, the internal volume for all the cases is kept constant, however, as a consequence, each case has a different building height and a different height of the windward facade, and also a different opening area (porosity). The building height and windward facade area could be important factors in the change in volume flow rate with roof inclination angle. Additional research is needed to study the effect of wall area above and below the inlet opening, and to better understand its effect on the overpressure region around the inlet opening and the consequences for the direction of the incoming flow.
- The simulations in this study are performed for an isothermal situation. Future work will focus on non-isothermal situations to study the effect of temperature gradients inside the building, the balance between wind and buoyancy as driving forces for the ventilation flow, and convective heat transfer inside the building.

8 Conclusions

This paper presents a CFD analysis to study the influence of the roof inclination angle and the vertical position of the outlet opening on the wind-driven cross-ventilation flow in a generic isolated low-rise building. CFD is

chosen for this study since the different roof geometries are assessed based on both the volume flow rates through the windows, and the airflow pattern (velocities) inside the building. The simulations are based on a grid-sensitivity analysis and on validation using Particle Image Velocimetry (PIV) wind-tunnel measurements. The main conclusions of this paper are:

- The validation study shows that the SST k-ω turbulence model provides the most accurate results, followed by the RNG k-ε turbulence model. The standard k-ε model, the realizable k-ε model, the standard k-ω model and the Reynolds Stress Model show larger deviations from the measured velocities.
- The influence of the parameter "a" for the calculation of the turbulent kinetic energy profiles at the inlet of the computational domain is tested. The results show that a value of 0.5 results in the best agreement with the wind-tunnel measurements.
- The volume flow rate depends on the roof inclination angle. The building with a 45° roof inclination angle (RIA_45) provides better results than all the other cases; the volume flow rate is 22% higher than for the reference case when the outlet opening is located at the same height as in the reference case; and the volume flow rate is 25% higher when the outlet opening is located near the roof.
- The indoor air flow pattern changes with changing roof inclination angle, which also influences the velocities at horizontal lines inside the building. It is shown that the angle under which the jet enters the building through the window changes (becomes more horizontal) with increasing roof inclination angle due to a different pressure distribution on the windward facade of the building. However, the non-dimensional area-averaged velocity magnitude ($|V|/U_{ref}$) in the occupied zone for the vertical center plane only exhibits small changes up to 7%. Larger changes are found when splitting up the occupied zone in a lower and an upper part.
- To improve the volume flow rate in the studied low-rise building the roof inclination angle must be larger than 18°. For smaller roof inclination angles, such as 9°, the volume flow rate is lower than for the same building with a flat roof (reference case). It seems that the windward facade area (height) at lower roof inclination angles (9° and 18°) has a significant impact on the indoor airflow patterns and volume flow rates.
- The vertical position of the outlet opening is less important as it is shown that it can just increase the volume flow rate by around 4% and 2% for case RIA_27_B and RIA_45_B, respectively. Furthermore, shifting the outlet opening to the top only provides small or no changes in non-dimensional ($|V|/U_{ref}$) average velocities in the occupied zone.
- Simulations for a sealed building for RIA_00 and RIA_45 show that the sealed-building pressure difference (ΔC_P) between the windward and leeward facade cannot be clearly related to the actual volume flow rates with "open" ventilation openings. This is attributed to differences in flow resistance in the different cases but especially to the invalidity of the sealed-body assumption.

9 Acknowledgements

This work was supported by The Coordination for the Improvement of Higher Level Personnel (CAPES), Brazil, The Engineering School of the University of São Paulo (USP), Brazil and the unit Building Physics and Services of the Department of the Built Environment at Eindhoven University of Technology in the Netherlands.

Twan van Hooff is currently a postdoctoral fellow of the Research Foundation – Flanders (FWO) and acknowledges its financial support (project FWO 12R9715N).

10 References

[1] Robbins CL. Daylighting: design and analysis. Van Nostrand Reinhold Company; 1986.
[2] Bittencourt L. Introdução à ventilação natural nas edificações. EDUFAL; 2006.
[3] Lima L, Bittencourt L, Cândido C, Oliveira J. Ventilação natural em edifícios escolares: avaliação da variação de altura de captadores de vento, São Paulo: 2004.
[4] Cândido C, Bittencourt L, Oliveira J, Fontan J. Avaliação da localização das aberturas de captadores de vento na ventilação natural de edificações escolares, São Paulo: 2004, p. 14.
[5] Bittencourt L, Cândido C, Batista J. A utilização de captadores de vento para aumentar a ventilação natural em espaços de sala de aula, Curitiba - PR - Brasil: 2003, p. 8.
[6] Stathopoulos T, Saathoff P. Codification of wind pressure coefficients for sawtooth roofs. J Wind Eng Ind Aerodyn 1992;43:1727–38. doi:16/0167-6105(92)90584-W.

[7] Perén JI. Ventilação e iluminação naturais na obra de João Filgueiras Lima “Lelé”: estudo dos hospitais da rede Sarah Kubitschek Fortaleza e Rio de Janeiro. Universidade de São Paulo, USP-São Carlos, 2006.
[8] Gandemer J, Barnaud G. Ventilation naturelle des habitations sous climat tropical humide: Aproach aerodynamique. Nantes: CSTB; 1989.
[9] Awbi HB. Ventilation Systems: Design and Performance. Routledge; 2007.
[10] Pierre LMS, Kopp GA, Surry D, Ho TCE. The UWO contribution to the NIST aerodynamic database for wind loads on low buildings: Part 2. Comparison of data with wind load provisions. J Wind Eng Ind Aerodyn 2005;93:31–59. doi:10.1016/j.jweia.2004.07.007.
[11] Quan Y, Tamura Y, Matsui M. Mean wind pressure coefficients on surfaces of gable-roofed low-rise buildings. Adv Struct Eng 2007;10:259–71. doi:10.1260/136943307781422253.
[12] Holmes JD. Wind pressures on tropical housing. J Wind Eng Ind Aerodyn 1994;53:105–23. doi:10.1016/0167-6105(94)90021-3.
[13] Holmes JD, Paterson DA. Mean wind pressures on arched-roof buildings by computation. J Wind Eng Ind Aerodyn 1993;50:235–42. doi:10.1016/0167-6105(93)90078-3.
[14] Stathopoulos T, Mohammadian AR. Modelling of wind pressures on monoslope roofs. Eng Struct 1991;13:281–92. doi:16/0141-0296(91)90039-F.
[15] Cui B. Wind effects on monosloped and sawtooth roof. PhD Thesis. Clemson University, 2007.
[16] Stathopoulos T, Wu H. Knowledge-based wind loading for envelope design: beyond building codes. J Wind Eng Ind Aerodyn 1994;53:177–88. doi:10.1016/0167-6105(94)90025-6.
[17] Prasad D, Uliate T, Ahmed MR. Wind loads on low-rise building models with different roof configurations. Int J Fluid Mech Res 2009;36:231–43. doi:10.1615/InterJFluidMechRes.v36.i3.30.
[18] Ohba M, Irie K, Kurabuchi T. Study on airflow characteristics inside and outside a cross-ventilation model, and ventilation flow rates using wind tunnel experiments. J Wind Eng Ind Aerodyn 2001;89:1513–24. doi:10.1016/S0167-6105(01)00130-1.
[19] Karava P, Stathopoulos T, Athienitis AK. Wind driven flow through openings – A review of discharge coefficients. Int J Vent 2004;3:255–66. doi:10.5555/ijov.2004.3.3.255.
[20] Hu C-H, Kurabuchi T, Ohba M. Numerical study of cross-ventilation using two-equation RANS turbulence models. Int J Vent 2005;4:123–32.
[21] Karava P, Stathopoulos T, Athienitis AK. Impact of internal pressure coefficients on wind-driven ventilation analysis. Int J Vent 2006;5:53–66.
[22] Asfour OS, Gadi MB. A comparison between CFD and network models for predicting wind-driven ventilation in buildings. Build Environ 2007;42:4079–85. doi:10.1016/j.buildenv.2006.11.021.
[23] Karava P. Airflow prediction in buildings for natural ventilation design: wind tunnel measurements and simulation. PhD thesis. Department of Building, Civil and Environmental Engineering, Concordia University, 2008.
[24] Hu C-H, Ohba M, Yoshie R. CFD modelling of unsteady cross ventilation flows using LES. J Wind Eng Ind Aerodyn 2008;96:1692–706. doi:10.1016/j.jweia.2008.02.031.
[25] Meroney RN. CFD prediction of airflow in buildings for natural ventilation. Proc. 11th Am. Conf. Wind Eng., San Juan, Puerto Rico: 2009, p. 1–11.
[26] Karava P, Stathopoulos T. Wind-induced internal pressures in buildings with large façade openings. J Eng Mech 2012;138:358–70. doi:10.1061/(ASCE)EM.1943-7889.0000296.
[27] Karava P, Stathopoulos T, Athienitis AK. Airflow assessment in cross-ventilated buildings with operable façade elements. Build Environ 2011;46:266–79. doi:10.1016/j.buildenv.2010.07.022.
[28] Chu C-R, Chiang B-F. Wind-driven cross ventilation in long buildings. Build Environ 2014;80:150–8. doi:10.1016/j.buildenv.2014.05.017.
[29] Ramponi R, Blocken B. CFD simulation of cross-ventilation flow for different isolated building configurations: Validation with wind tunnel measurements and analysis of physical and numerical diffusion effects. J Wind Eng Ind Aerodyn 2012;104–106:408–18. doi:10.1016/j.jweia.2012.02.005.
[30] Ramponi R, Blocken B. CFD simulation of cross-ventilation for a generic isolated building: Impact of computational parameters. Build Environ 2012;53:34–48. doi:10.1016/j.buildenv.2012.01.004.
[31] Karava P, Stathopoulos T, Athienitis AK. Wind-induced natural ventilation analysis. Sol Energy 2007;81:20–30. doi:10.1016/j.solener.2006.06.013.
[32] Kobayashi T, Sandberg M, Kotani H, Claesson L. Experimental investigation and CFD analysis of cross-ventilated flow through single room detached house model. Build Environ 2010;45:2723–34. doi:10.1016/j.buildenv.2010.06.001.
[33] Kindangen J, Krauss G. Investigation of natural ventilation with Computational Fluid Dynamics: A comparison study with wind tunnel results. Archit Sci Rev 1996;39:113–20. doi:10.1080/00038628.1996.9697366.
[34] Kindangen J, Krauss G, Depecker P. Effects of roof shapes on wind-induced air motion inside buildings. Build Environ 1997;32:1–11.

[35] Kindangen JI. Window and roof configurations for comfort ventilation. Build Res Inf 1997;25:218–25. doi:10.1080/096132197370345.
[36] Bartzanas T, Boulard T, Kittas C. Numerical simulation of the airflow and temperature distribution in a tunnel greenhouse equipped with insect-proof screen in the openings. Comput Electron Agric 2002;34:207–21. doi: 10.1016/S0168-1699(01)00188-0.
[37] Mistriotis A, Bot GPA, Picuno P, Scarascia-Mugnozza G. Analysis of the efficiency of greenhouse ventilation using computational fluid dynamics. Agric For Meteorol 1997;85:217–28. doi:10.1016/S0168-1923(96)02400-8.
[38] Mistriotis A, Arcidiacono C, Picuno P, Bot GPA, Scarascia-Mugnozza G. Computational analysis of ventilation in greenhouses at zero- and low-wind-speeds. Agric For Meteorol 1997;88:121–35. doi:10.1016/S0168-1923(97)00045-2.
[39] Bartzanas T, Boulard T, Kittas C. Effect of vent arrangement on windward ventilation of a tunnel greenhouse. Biosyst Eng 2004;88:479–90. doi:10.1016/j.biosystemseng.2003.10.006.
[40] Shklyar A, Arbel A. Numerical model of the three-dimensional isothermal flow patterns and mass fluxes in a pitched-roof greenhouse. J Wind Eng Ind Aerodyn 2004;92:1039–59. doi:10.1016/j.jweia.2004.05.008.
[41] Norton T, Grant J, Fallon R, Sun D-W. Assessing the ventilation effectiveness of naturally ventilated livestock buildings under wind dominated conditions using computational fluid dynamics. Biosyst Eng 2009;103:78–99. doi:10.1016/j.biosystemseng.2009.02.007.
[42] Norton T, Grant J, Fallon R, Sun D-W. Optimising the ventilation configuration of naturally ventilated livestock buildings for improved indoor environmental homogeneity. Build Environ 2010;45:983–95. doi:10.1016/j.buildenv.2009.10.005.
[43] Kobayashi T, Chikamoto T, Osada K. Evaluation of ventilation performance of monitor roof in residential area based on simplified estimation and CFD analysis. Build Environ 2013;63:20–30. doi:10.1016/j.buildenv.2013.01.018.
[44] Gerhardt HJ, Kramer C. Aerodynamic efficiency of smoke ventilators in light streets and shed-type roofs. J Wind Eng Ind Aerodyn 1993;45:341–53. doi:10.1016/0167-6105(93)90105-W.
[45] Fatnassi H, Boulard T, Poncet C, Chave M. Optimisation of greenhouse insect screening with Computational Fluid Dynamics. Biosyst Eng 2006;93:301–12. doi:10.1016/j.biosystemseng.2005.11.014.
[46] Montero JI, Hunt GR, Kamaruddin R, Antón A, Bailey BJ. SE—Structures and environment: Effect of ventilator configuration on wind-driven ventilation in a crop protection structure for the tropics. J Agric Eng Res 2001;80:99–107. doi:10.1006/jaer.2000.0694.
[47] van Hooff T, Blocken B. Coupled urban wind flow and indoor natural ventilation modelling on a high-resolution grid: A case study for the Amsterdam Arena stadium. Environ Model Softw 2010;25:51–65. doi:10.1016/j.envsoft.2009.07.008.
[48] van Hooff T, Blocken B. On the effect of wind direction and urban surroundings on natural ventilation of a large semi-enclosed stadium. Comput Fluids 2010;39:1146–55. doi:10.1016/j.compfluid.2010.02.004.
[49] van Hooff T, Blocken B. Full-scale measurements of indoor environmental conditions and natural ventilation in a large semi-enclosed stadium: Possibilities and limitations for CFD validation. J Wind Eng Ind Aerodyn 2012;104-106:330–41. doi:10.1016/j.jweia.2012.02.009.
[50] van Hooff T, Blocken B. CFD evaluation of natural ventilation of indoor environments by the concentration decay method: CO_2 gas dispersion from a semi-enclosed stadium. Build Environ 2013;61:1–17. doi:10.1016/j.buildenv.2012.11.021.
[51] Cruz-Salas MV, Castillo JA, Huelsz G. Experimental study on natural ventilation of a room with a windward window and different wind exchangers. Energy Build 2014;84:458–65. doi:10.1016/j.enbuild.2014.08.033.
[52] Karakatsanis C, Bahadori MN, Vickery BJ. Evaluation of pressure coefficients and estimation of air flow rates in buildings employing wind towers. Sol Energy 1986;37:363–74. doi:10.1016/0038-092X(86)90132-5.
[53] Horan JM, Finn DP. Sensitivity of air change rates in a naturally ventilated atrium space subject to variations in external wind speed and direction. Energy Build 2008;40:1577–85. doi:10.1016/j.enbuild.2008.02.013.
[54] Asfour OS, Gadi MB. Using CFD to investigate ventilation characteristics of vaults as wind-inducing devices in buildings. Appl Energy 2008;85:1126–40. doi:10.1016/j.apenergy.2007.10.015.
[55] Montazeri H, Azizian R. Experimental study on natural ventilation performance of one-sided wind catcher. Build Environ 2008;43:2193–202. doi:10.1016/j.buildenv.2008.01.005.
[56] Montazeri H, Azizian R. Experimental study on natural ventilation performance of a two-sided wind catcher. Proc Inst Mech Eng Part J Power Energy 2009;223:387–400. doi:10.1243/09576509JPE651.
[57] Montazeri H, Montazeri F, Azizian R, Mostafavi S. Two-sided wind catcher performance evaluation using experimental, numerical and analytical modeling. Renew Energy 2010;35:1424–35. doi:10.1016/j.renene.2009.12.003.

[58] Montazeri H. Experimental and numerical study on natural ventilation performance of various multi-opening wind catchers. Build Environ 2011;46:370–8. doi:10.1016/j.buildenv.2010.07.031.
[59] van Hooff T, Blocken B, Aanen L, Bronsema B. A venturi-shaped roof for wind-induced natural ventilation of buildings: Wind tunnel and CFD evaluation of different design configurations. Build Environ 2011;46:1797–807. doi:16/j.buildenv.2011.02.009.
[60] Blocken B, van Hooff T, Aanen L, Bronsema B. Computational analysis of the performance of a venturi-shaped roof for natural ventilation: venturi-effect versus wind-blocking effect. Comput Fluids 2011;48(1): 202-213.
[61] Chu CR, Chiu Y-H, Chen Y-J, Wang Y-W, Chou C-P. Turbulence effects on the discharge coefficient and mean flow rate of wind-driven cross-ventilation. Build Environ 2009;44:2064-2072.
[62] True JJ, Sandberg M, Heiselberg P, Nielsen PV. Wind driven cross-flow analyzed as a catchment problem and as a pressure driven flow. Int J Vent 2003;1:88–102.
[63] Kato S, Murakami S, Mochida A, Akabayashi S, Tominaga Y. Velocity-pressure field of cross ventilation with open windows analyzed by wind tunnel and numerical simulation. J Wind Eng Ind Aerodyn 1992;44:2575–86. doi:10.1016/0167-6105(92)90049-G.
[64] Blocken B. 50 years of Computational Wind Engineering: Past, present and future. J Wind Eng Ind Aerodyn 2014;129:69–102. doi:10.1016/j.jweia.2014.03.008.
[65] Stathopoulos T. Computational wind engineering: Past achievements and future challenges. J Wind Eng Ind Aerodyn 1997;67–68:509–32. doi:10.1016/S0167-6105(97)00097-4.
[66] Blocken B, Carmeliet J. A review of wind-driven rain research in building science. J Wind Eng Ind Aerodyn 2004;92:1079–130. doi:10.1016/j.jweia.2004.06.003.
[67] Mochida A, Lun IYF. Prediction of wind environment and thermal comfort at pedestrian level in urban area. J Wind Eng Ind Aerodyn 2008;96:1498–527. doi:10.1016/j.jweia.2008.02.033.
[68] Chen Q. Ventilation performance prediction for buildings: A method overview and recent applications. Build Environ 2009;44:848–58. doi:10.1016/j.buildenv.2008.05.025.
[69] Blocken B, Stathopoulos T, Carmeliet J, Hensen JLM. Application of computational fluid dynamics in building performance simulation for the outdoor environment: An overview. J Build Perform Simul 2011;4:157–84. doi:10.1080/19401493.2010.513740.
[70] Moonen P, Defraeye T, Dorer V, Blocken B, Carmeliet J. Urban physics: effect of the microclimate on comfort, health and energy demand. Front Arch Res 2012;1:197–228.
[71] Tominaga Y, Stathopoulos T. CFD simulation of near-field pollutant dispersion in the urban environment: A review of current modeling techniques. Atmos Environ 2013;79:716–30. doi:10.1016/j.atmosenv.2013.07.028.
[72] Jiang Y, Alexander D, Jenkins H, Arthur R, Chen Q. Natural ventilation in buildings: measurement in a wind tunnel and numerical simulation with large-eddy simulation. J Wind Eng Ind Aerodyn 2003;91:331–53. doi:10.1016/S0167-6105(02)00380-X.
[73] Stathopoulos T. Design and fabrication of a wind tunnel for building aerodynamics. J Wind Eng Ind Aerodyn 1984;16:361–76. doi:10.1016/0167-6105(84)90018-7.
[74] Blocken B, Stathopoulos T, Carmeliet J. Wind environmental conditions in passages between two long narrow perpendicular buildings. J Aerosp Eng 2008;21:280–7. doi:10.1061/(ASCE)0893-1321(2008)21:4(280).
[75] Blocken B, Moonen P, Stathopoulos T, Carmeliet J. Numerical study on the existence of the venturi effect in passages between perpendicular buildings. J Eng Mech 2008;134:1021–8. doi:10.1061/(ASCE)0733-9399(2008)134:12(1021).
[76] Franke J, Hellsten A, Schlünzen H, Carissimo B. Best practice guideline for the CFD simulation of flows in the urban environment. Brussels: COST Office 2007.
[77] Tominaga Y, Mochida A, Yoshie R, Kataoka H, Nozu T, Yoshikawa M, et al. AIJ guidelines for practical applications of CFD to pedestrian wind environment around buildings. J Wind Eng Ind Aerodyn 2008;96:1749–61. doi:16/j.jweia.2008.02.058.
[78] Blocken B, Stathopoulos T, Carmeliet J. CFD simulation of the atmospheric boundary layer: wall function problems. Atmos Environ 2007;41:238–52. doi:16/j.atmosenv.2006.08.019.
[79] Blocken B, Carmeliet J, Stathopoulos T. CFD evaluation of wind speed conditions in passages between parallel buildings—effect of wall-function roughness modifications for the atmospheric boundary layer flow. J Wind Eng Ind Aerodyn 2007;95:941–62. doi:10.1016/j.jweia.2007.01.013.
[80] Gousseau P, Blocken B, Stathopoulos T, van Heijst GJF. CFD simulation of near-field pollutant dispersion on a high-resolution grid: A case study by LES and RANS for a building group in downtown Montreal. Atmos Environ 2011;45:428–38. doi:10.1016/j.atmosenv.2010.09.065.
[81] van Hooff T, Blocken B, van Harten M. 3D CFD simulations of wind flow and wind-driven rain shelter in sports stadia: Influence of stadium geometry. Build Environ 2011;46:22–37. doi:10.1016/j.buildenv.2010.06.013.

[82] Blocken B, Janssen WD, van Hooff T. CFD simulation for pedestrian wind comfort and wind safety in urban areas: General decision framework and case study for the Eindhoven University campus. Environ Model Softw 2012;30:15–34. doi:10.1016/j.envsoft.2011.11.009.
[83] Montazeri H, Blocken B, Janssen WD, van Hooff T. CFD evaluation of new second-skin facade concept for wind comfort on building balconies: Case study for the Park Tower in Antwerp. Build Environ 2013;68:179–92. doi:10.1016/j.buildenv.2013.07.004.
[84] Launder BE, Spalding DB. The numerical computation of turbulent flows. Comput Methods Appl Mech Eng 1974;3:269–89. doi:10.1016/0045-7825(74)90029-2.
[85] Cebeci T, Bradshaw P. Momentum transfer in boundary layers. Hemisphere Publishing Corp. New York: 1977.
[86] Menter FR. Two-equation eddy-viscosity turbulence models for engineering applications. AIAA J 1994;32:1598–605.
[87] ANSYS. Fluent 12 user's guide. Lebanon: Fluent Inc. 2009.
[88] Launder BE, Spalding DB. Lectures in mathematical models of turbulence. Academic Press, London, England, 1972.
[89] Shih TH, Liou WW, Shabbir A, Yang Z, Zhu J. A new k-e eddy viscosity model for high Reynolds number turbulent flows. Comput Fluids 1995;24:227–38.
[90] Yakhot V, Orszag SA, Thangam S, Gatski TB, Speziale CG. Development of turbulence models for shear flows by a double expansion technique. Phys Fluids Fluid Dyn 1992;4:1510–20. doi:doi:10.1063/1.858424.
[91] Choudhury D. Introduction to the renormalization group method and turbulence modeling. 1993.
[92] Wilcox DC. Turbulence modeling for CFD. California: DCW Industries, Inc.; 1993.
[93] Launder BE, Reece GJ, Rodi W. Progress in the development of a Reynolds-stress turbulence closure. J Fluid Mech 1975;68:537–66. doi:10.1017/S0022112075001814.
[94] Lo LJ, Novoselac A. Cross ventilation with small openings: Measurements in a multi-zone test building. Build Environ 2012;57:377–86. doi:10.1016/j.buildenv.2012.06.009.
[95] Straw MP. Computation and measurement of wind induced ventilation. PhD thesis. University of Nottingham, UK, 2000.

TABLES

Table 1. Overview of computational parameters for sensitivity analysis with indication of the reference case in bold.

	Computational grid resolution (Subsection 5.1)	Turbulence models (Subsection 5.2)	Turbulent kinetic energy (Subsection 5.3)
Reference case	**770,540 cells (Average)**	**SST k-ω** [84] Sk-ε [86] Rk-ε [87] RNG k-ε [88,89] Sk-ω [90] RSM [91]	**a = 0.5** a = 1 a = 1.5
	421,088 cells (Coarse)	-	-
	1,607,572 cells (Fine)	-	-

Table 2. Parameters of the leeward sawtooth roof sensitivity analysis with indication of the reference case.

	Building case name	Roof inclination angle	Outlet opening position case	
			Case A	Case B
			(Section 6.1)	(Section 6.2)
Ref. case	**RIA_00 (Karava)**	**0°**	**X**	
	RIA_09	9°	X	
	RIA_18	18°	X	
	RIA_27	27°	X	X
	RIA_36	36°	X	
	RIA_45	45°	X	X

Table 3. Non-dimensional area-averaged velocity magnitude ($|V|/U_{ref}$) in the occupied zone in the vertical center plane for the different roof inclination angles.

Building case name	$|V|/U_{ref}$ in the occupied zone in the vertical center plane		
	Entire occupied zone	Lower part	Upper part
RIA_00	0.29	0.41	0.22
RIA_09	0.31	0.45	0.23
RIA_18	0.29	0.39	0.22
RIA_27	0.33	0.41	0.28
RIA_36	0.32	0.38	0.29
RIA_45	0.32	0.29	0.34

Table 4. Non-dimensional area-averaged velocity magnitude ($|V|/U_{ref}$) in the occupied zone in the vertical center plane for the different leeward window opening locations.

Building case name	$|V|/U_{ref}$ in the occupied zone in the vertical center plane		
	Entire occupied zone	Lower part	Upper part
RIA_27_A	0.33	0.41	0.28
RIA_27_B	0.35	0.42	0.30
RIA_45_A	0.32	0.29	0.34
RIA_45_B	0.32	0.27	0.36

Table 5. Pressure coefficients (C_P) obtained from CFD simulations of a sealed building. Values reported are average C_P values over the window surface.

Building case name	Pressure coefficient C_P [-]		
	$C_{P;w}$ (windward)	$C_{P;l}$ (leeward)	ΔC_P
RIA_00 (Karava)	0.84	-0.31	1.15
RIA_45_A	0.78	-0.53	1.31
RIA_45_B	0.78	-0.46	1.24

FIGURES

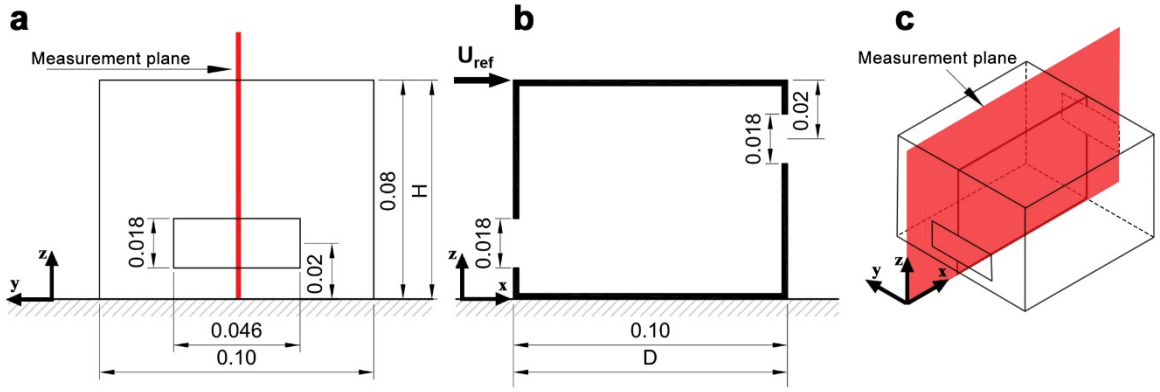

Fig.1. (a) Front view of the reduced-scaled building model as studied by Karava et al. [30] with opening size and dimensions (in meters). (b) Vertical cross-section of the reduced-scaled building model with opening size and dimensions (in meters). (c) Perspective indicating the measurement plane.

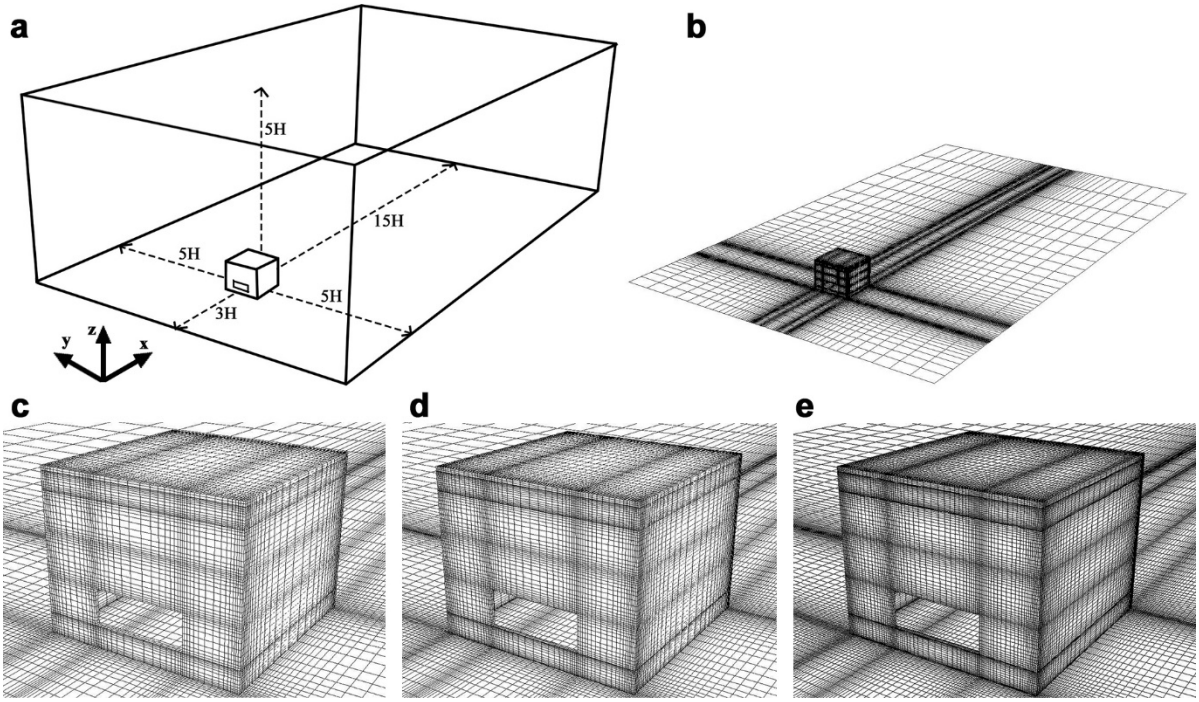

Fig. 2. (a) Perspective view of the building in its computational domain at model scale. (b) View of the computational grid (building and ground). (c,d,e) Perspective view of grids for the grid-sensitivity analysis: (c) Coarse grid with 421,088 cells; (d) Basic grid with 770,540 cells (reference case); (e) Fine grid with 1,607,572 cells.

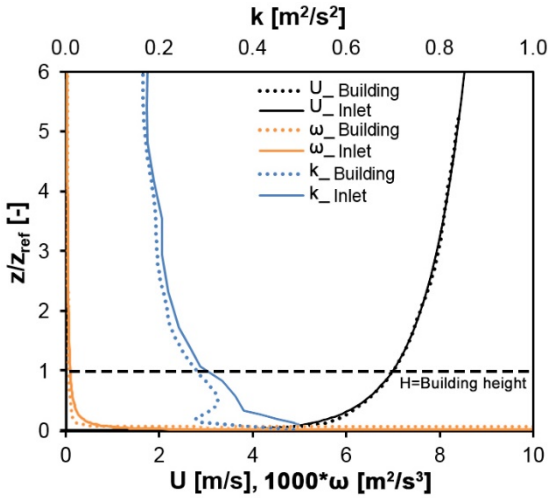

Fig. 3. Horizontal homogeneity analysis: Profiles of the mean wind speed (U), turbulent kinetic energy (k) and specific dissipation rate (ω) at the inlet (continuous lines) and at the building position (dotted lines) in the empty domain. The height of the model (Z_{ref}) is 0.08 m. The parameter a = 0.5 is used for the turbulent kinetic energy calculation (reference case).

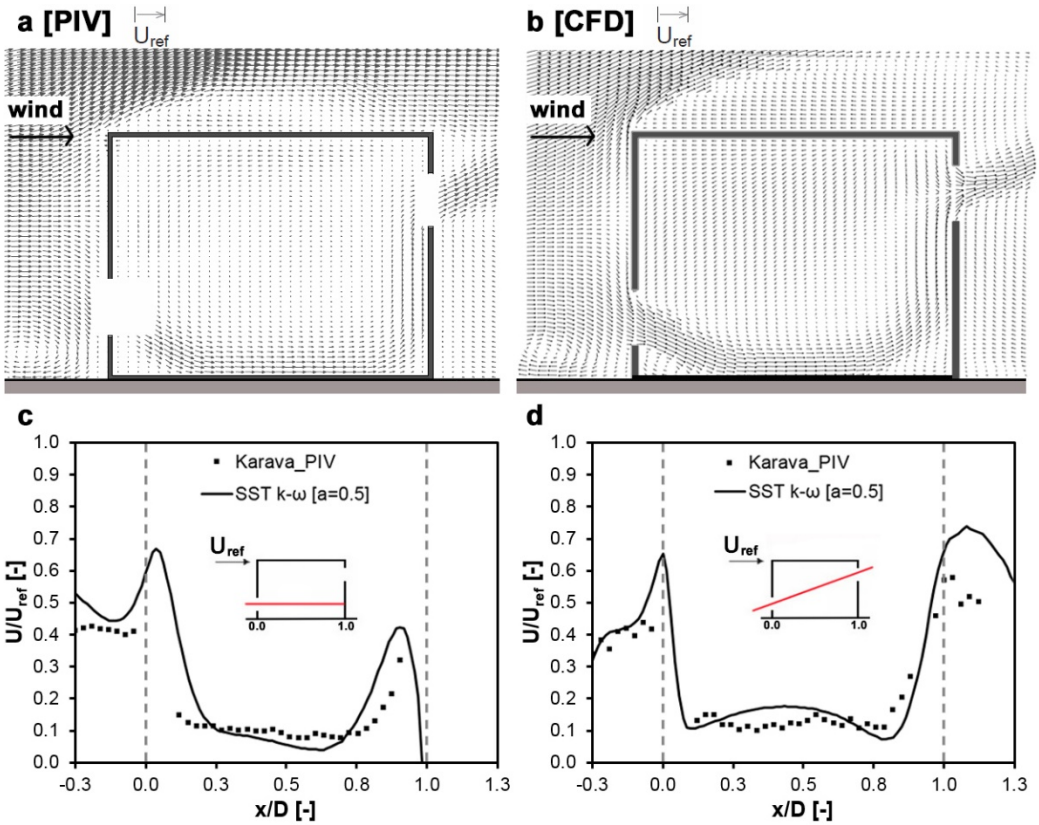

Fig. 4. (a,b) Comparison of the mean velocity in the vertical center plane obtained from: (a) PIV measurements (processed from [30]); (b) CFD simulations. (c,d) Streamwise wind speed ratio U/U_{ref} along (c) horizontal line and (d) diagonal line.

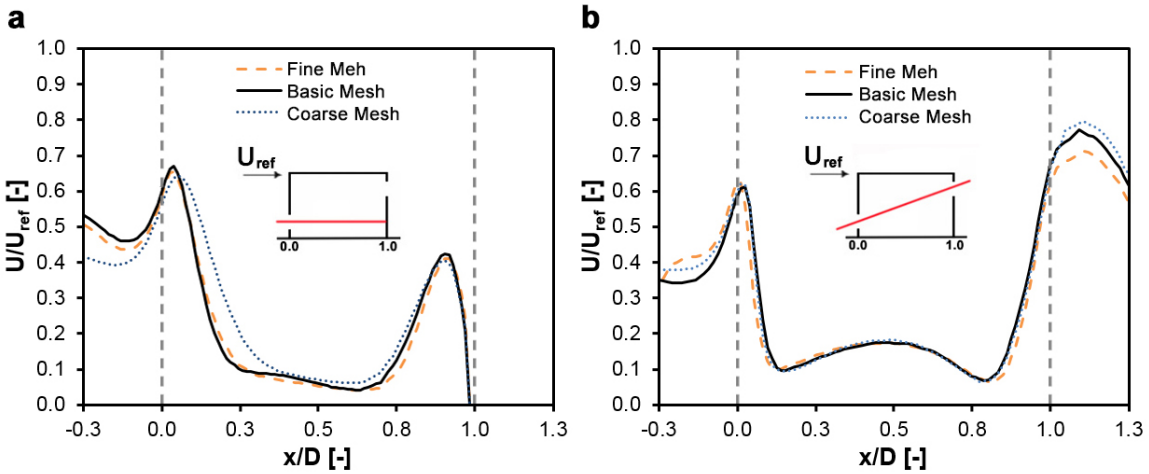

ig. 1.

Fig.5. Impact of grid resolution. (a) U/U_{ref} along a horizontal centerline. (b) U/U_{ref} along a diagonal line.

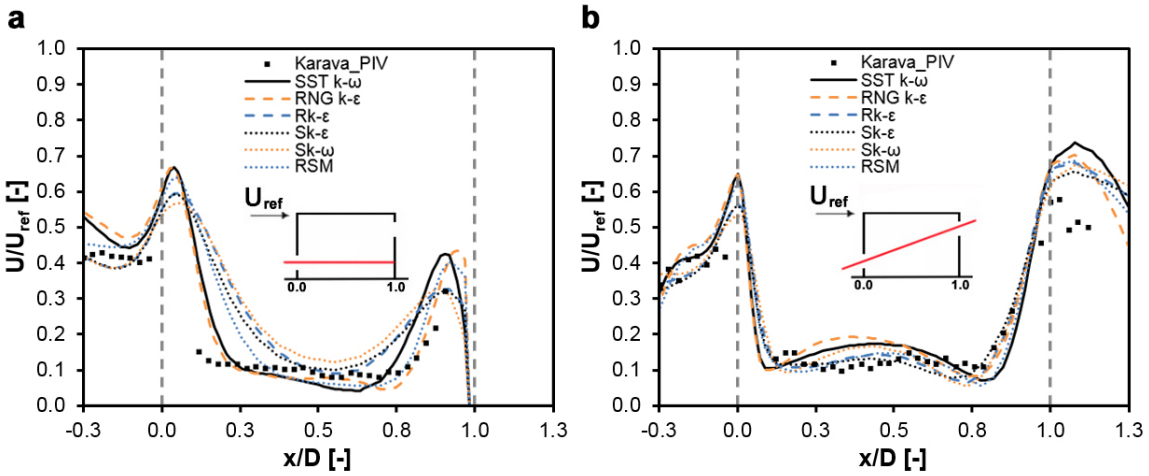

Fig. 6. Impact of turbulence model Comparison between PIV experiments [30] and CFD with the SST k- ω, RNG k-ε, Realizable k-ε, Standard k-ε, Standard k-ω, and RSM model. (a) U/U_{ref} along a horizontal centerline; (b) U/U_{ref} along a diagonal line.

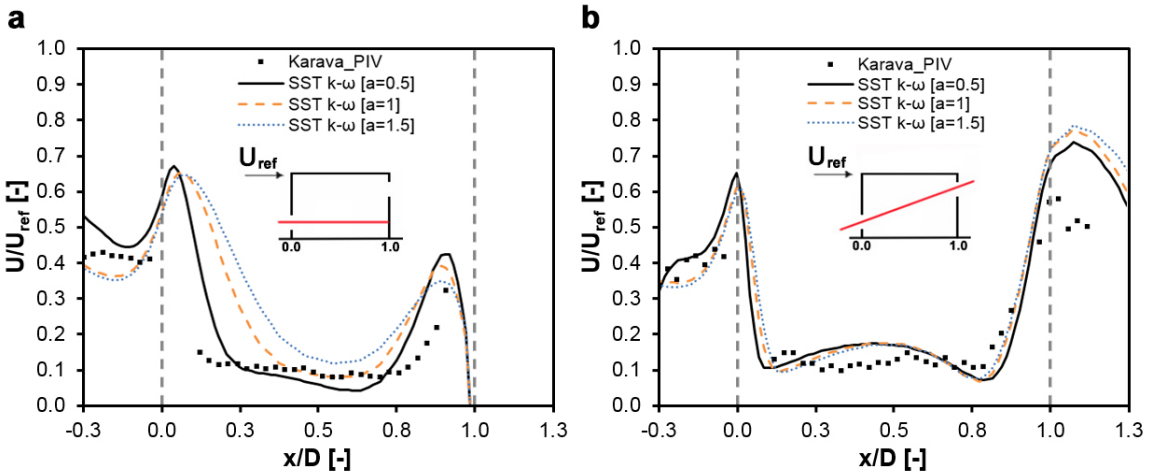

Fig. 7. Impact of inlet turbulent kinetic energy profile parameter a: (a) U/U_{ref} along a horizontal centerline. (b) U/U_{ref} along a diagonal line.

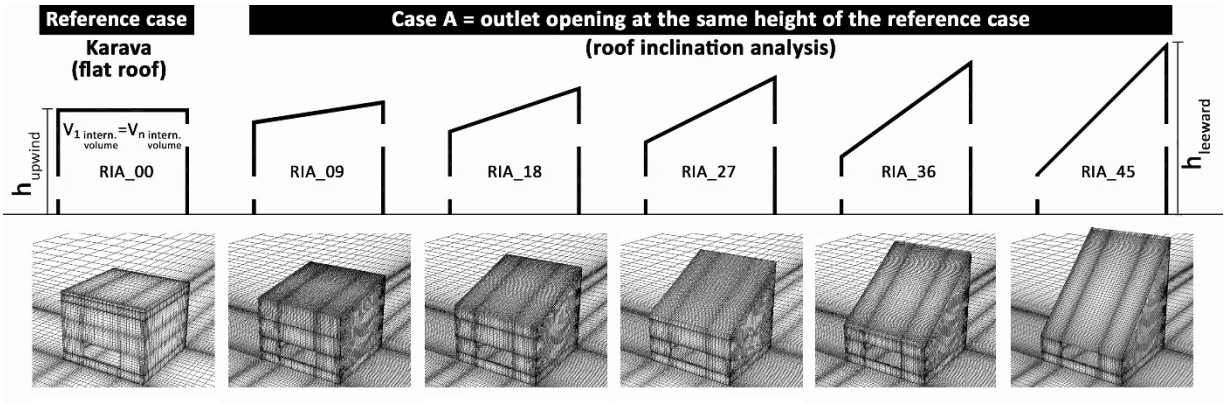

Fig. 8. Vertical cross-section and computational grid for building geometries iwith different roof inclination angle for the "basic case", i.e. with outlet opening at the same height as in the reference case. All the cases have the same internal volume as the reference case and as a consequence have different heights of the windward (h_{upwind}) and leeward facade ($h_{leeward}$).

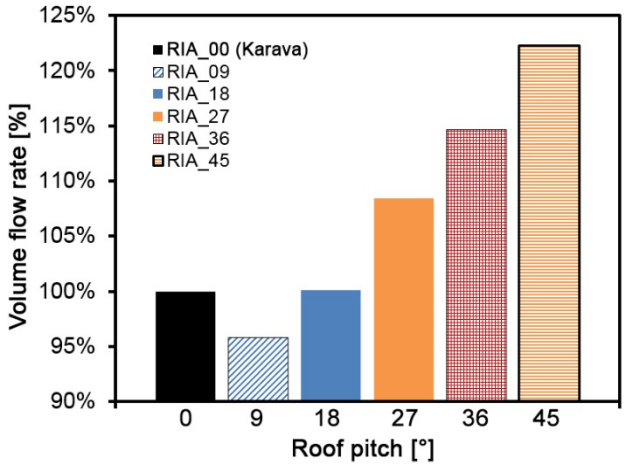

Fig. 9. Influence of roof inclination angle (RIA) on the volume flow rate.

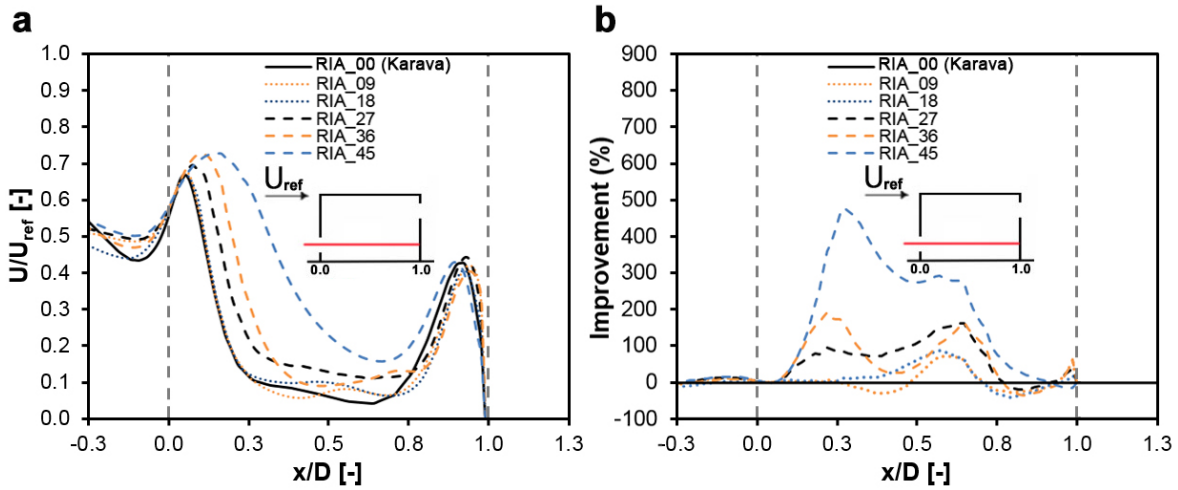

Fig. 10. Influence of roof inclination angle. (a) U/U_{ref} along a horizontal centerline (b) Percentage increase in wind speed along the same line.

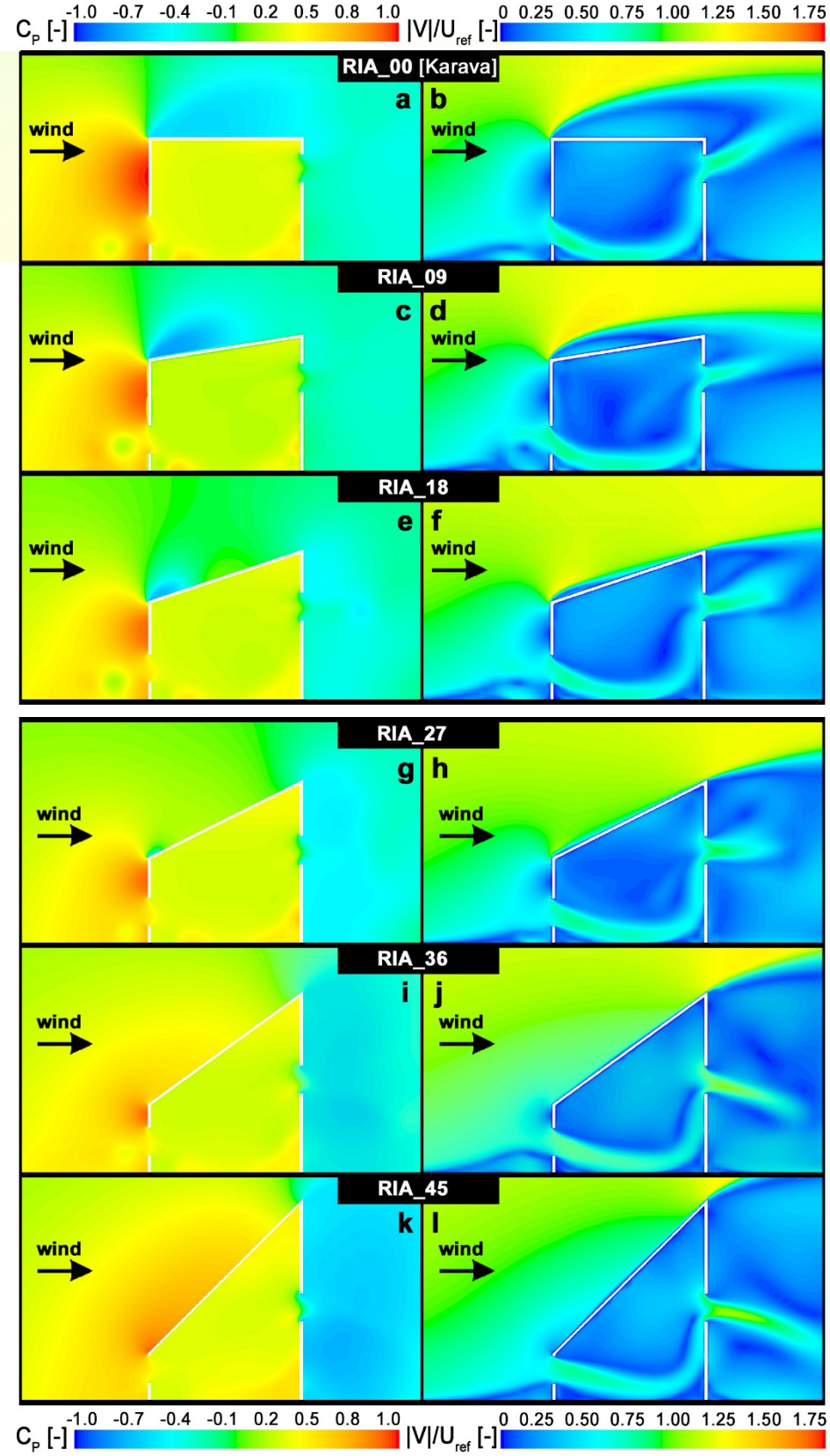

Fig. 11. (a,c,e,g,i,k) Contours of pressure coefficient C_P in vertical center plane (b,d,f,h,j,l) Contours of non-dimensional velocity magnitude ($|V|/U_{ref}$) in vertical center plane.

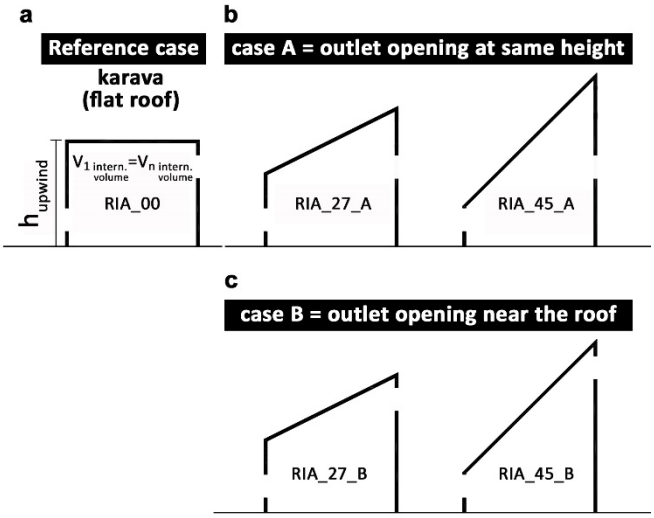

Fig. 12. Vertical cross-section of the geometries of: (a) case RIA_00 (reference case); (b) A cases with outlet opening at the same height as the reference case: RIA_27_A and RIA_45_A; (c) B cases, with outlet opening near the roof: RIA_27_B and RIA_45_B

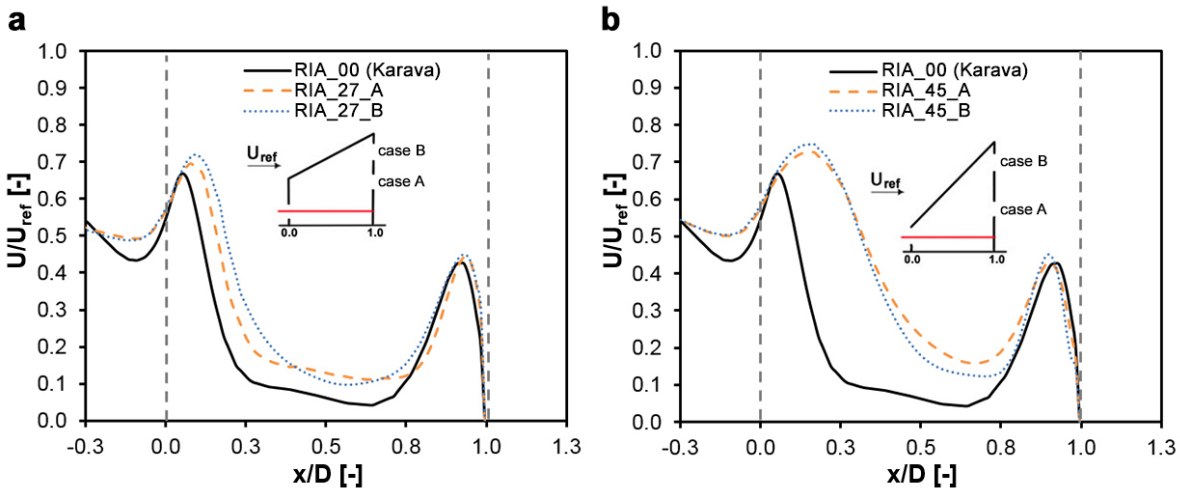

Fig. 13. Influence of the outlet opening position on the indoor air velocity along a horizontal centerline. (a) RIA_27_B. (b) RIA_45_B.

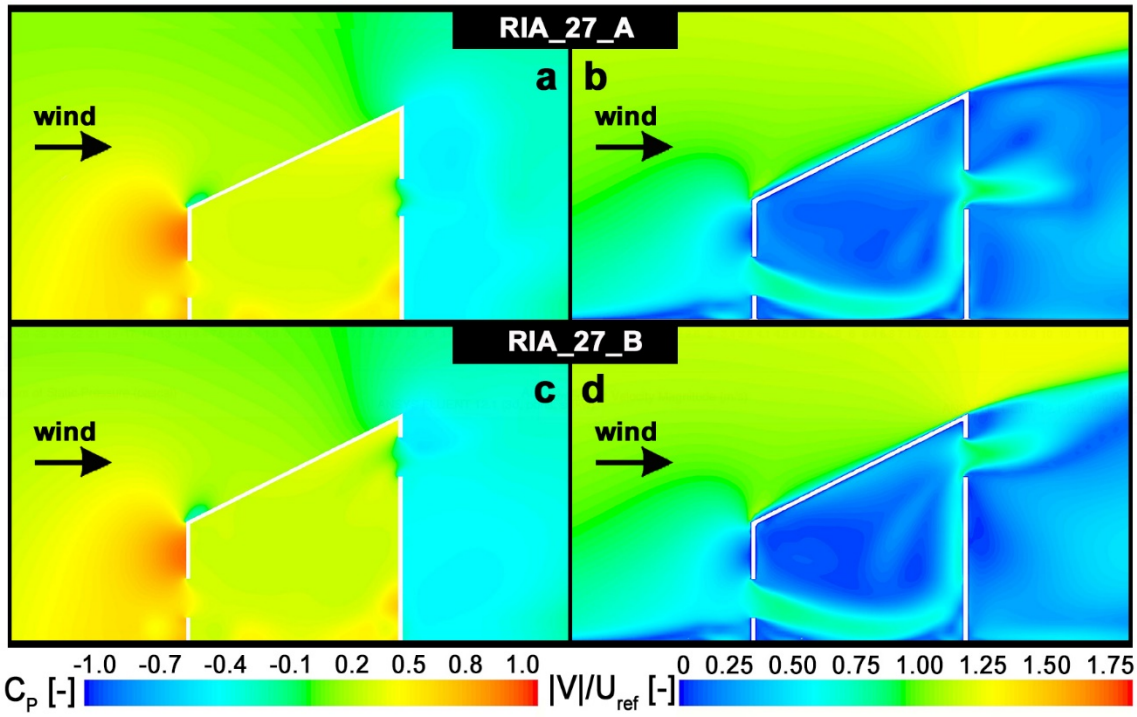

Fig. 14. Impact of the outlet opening location: (a,b) RIA_27_A and (c,d) RIA_27_B. (a,c) Contours of pressure coefficient C_P in the vertical centerplane. (b,d) Contours of non-dimensional velocity magnitude ($|V|/U_{ref}$) in the vertical centerplane.

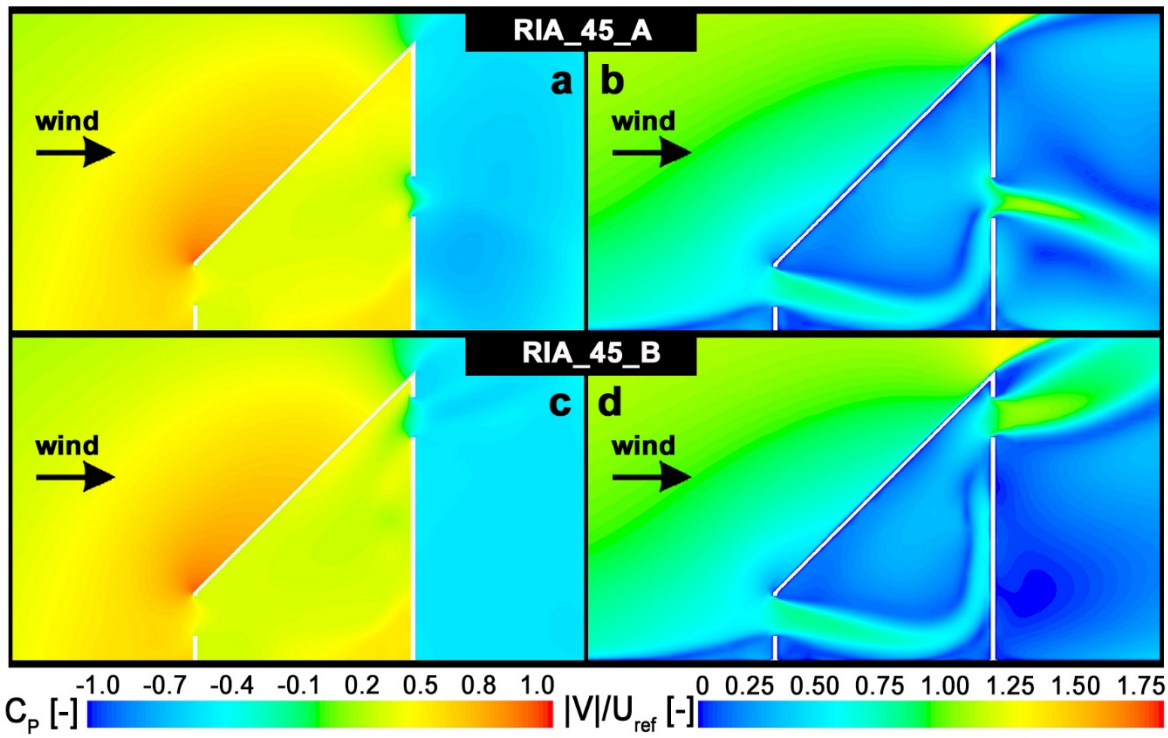

Fig. 15. Impact of the outlet opening location for (a,b) RIA_45_A and (c,d) RIA_45_B. (a,c) Contours of pressure coefficient C_P in the vertical centerplane. (b,d) Contours of non-dimensional velocity magnitude ($|V|/U_{ref}$) in the vertical centerplane.